MXene-Derived Bilayered Vanadium Oxides with Enhanced Stability in Li-Ion Batteries

*Phillip Ridley[1], Cyra Gallano[1], Ryan Andris[1], Christopher E. Shuck[2], Yury Gogotsi[2], Ekaterina Pomerantseva[1]**

[1] Department of Materials Science and Engineering, Drexel University, Philadelphia, PA 19104, USA

[2] A.J. Drexel Nanomaterials Institute and Department of Materials Science and Engineering, Drexel University, Philadelphia, PA 19104, USA

* Corresponding Author: Email: ep423@drexel.edu

Keywords: *sol-gel synthesis; V_2CT_x MXene; bilayered vanadium oxide; modification of anionic sublattice; Li-ion batteries*

Abstract

Bilayered vanadium oxide is a high-capacity intercalation host with affinity for various ions in energy storage systems. However, the electrochemical stability of bilayered vanadium oxide upon extended galvanostatic cycling, especially at high rates, is lackluster. In this study, we demonstrate transformative synthesis of chemically preintercalated bilayered vanadium oxides with unique two-dimensional (2D) morphology and improved electrochemical stability by oxidation of V_2CT_x MXene in hydrogen peroxide in the presence of alkali and alkaline-earth metal chlorides. The structure and composition of V_2CT_x-derived δ-$M_xV_2O_5{\cdot}nH_2O$ (M = Li, Na, K, Mg, Ca) phases were examined with X-ray diffraction, Raman spectroscopy, and scanning electron microscopy. The electrochemical properties of the V_2CT_x-derived δ-$Li_xV_2O_5{\cdot}nH_2O$ and δ-$Mg_xV_2O_5{\cdot}nH_2O$ electrodes in Li-ion cells were studied. Both materials exhibited high reversible specific capacity, improved cycling stability, and excellent rate capability. Notably, an enhanced tolerance to high current rates is observed with specific discharge capacity dropping from 200 $mAh{\cdot}g^{-1}$ to 130 $mAh{\cdot}g^{-1}$ and from 192 $mAh{\cdot}g^{-1}$ to 146 $mAh{\cdot}g^{-1}$ when the current rate was changed from C/10 to 5C in the case of V_2CT_x-derived δ-$Li_xV_2O_5{\cdot}nH_2O$ and δ-$Mg_xV_2O_5{\cdot}nH_2O$ electrodes, respectively. The improved capacity retention during electrochemical cycling may be attributed to the 2D morphology and improved crystallinity of the material enabled by the synthesis route.

Graphical Abstract

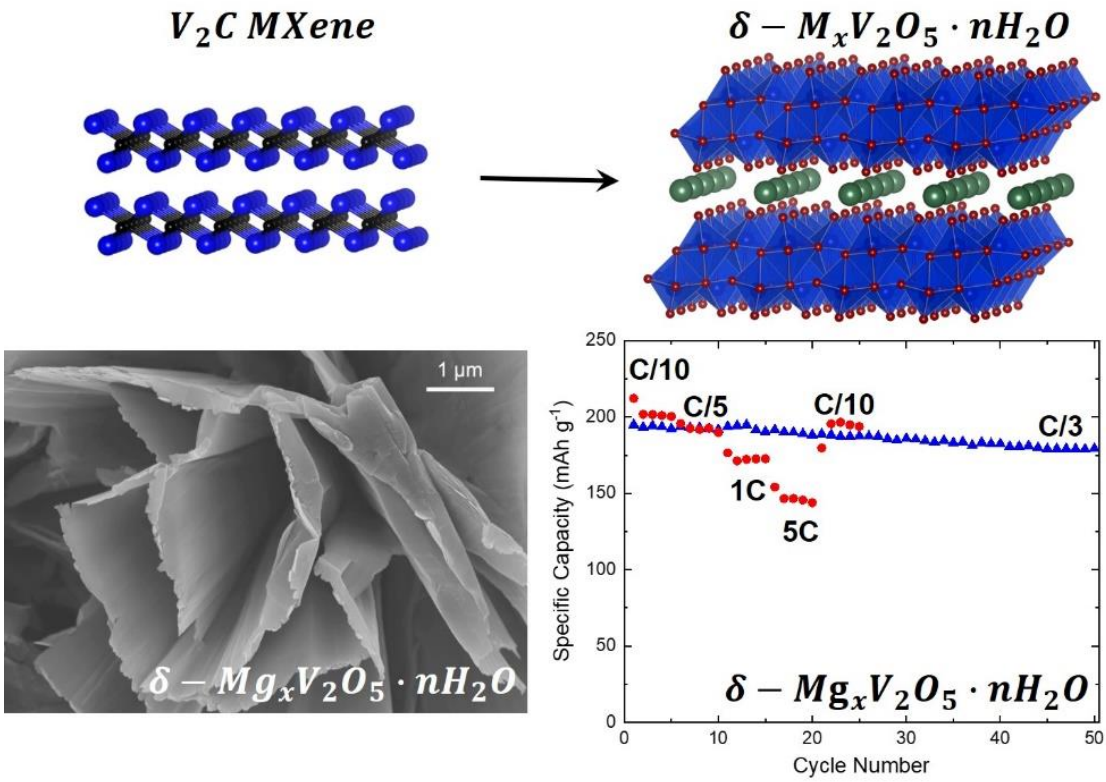

1. Introduction

Intercalation-based energy storage systems, such as Li-ion batteries (LIBs), have revolutionized energy storage, powering portable electronics, electric vehicles, and providing stationary grid storage, yet, there is an ever-increasing need for batteries that simultaneously store more energy, have longer lifetimes and enable faster charging. Transition metal compounds with layered nanoarchitectures are attractive candidates for electrodes in these systems due to their high surface area to volume ratio, fast diffusion speeds, and tailorable interlayer spacing [1-4]. Within intercalation-based chemistry regime, transition metals with multiple oxidation states, such as vanadium, niobium, or molybdenum, are preferred as the redox active species because they can undergo several reduction steps leading to the intercalation of multiple Li^+ ions per unit cell. However, larger numbers of intercalated Li^+ ions require much free space in the interlayer region. Therefore, larger interlayer distances are needed, which lead to weakened van der Waals forces and subsequently worsened structural and electrochemical stability. To counteract this, stabilizing, or pillaring, species must be incorporated into the interlayer region prior to electrochemical cycling to strengthen the lamellar bonding in the electrode. In addition to the transition metal ion, the anionic sublattice affects the intercalation potentials, establishing whether the material is suitable as a cathode or an anode.

δ- or bilayered vanadium oxide (BVO) is one promising material that satisfies all the above criteria [5-6]. The Li^+ ion intercalation potential into BVO electrodes is relatively high, making it attractive as a cathode for LIBs. The reduction of vanadium from the +5 oxidation state in the pristine material to +3 corresponds to the intercalation of two Li^+ ions per one vanadium redox center with the theoretical specific capacity of 294 $mAh \cdot g^{-1}$. The layered structure of δ-V_2O_5 is characterized by spacious galleries containing water molecules with a d-spacing of 11.5 Å, where d-spacing is defined as a distance between the centers of V-O layers. Therefore, the correct chemical formula of this material is δ-$V_2O_5 \cdot nH_2O$. BVO electrodes demonstrated high electrochemical performance for both Li-ion and other batteries, since the wide interlayer region can accommodate large ions, such as sodium or potassium, during cycling and there could be shielding effect for highly charged species in the case of magnesium and zinc ions due to the presence of water in the interlayer region [6-26]. Additionally, vanadium is more abundant than cobalt in Earth's crust, and therefore vanadium-based chemistries could be an interesting alternative to the conventional cobalt-based cathode compositions [27].

The capacity of δ-$V_2O_5 \cdot nH_2O$, while initially high, was shown to decay as the electrodes are cycled at constant or increasing current densities [10, 17, 24]. Three approaches that have been shown to enhance capacity retention are (i) pillaring with ions [26], (ii) low-temperature annealing [28] and (iii) formation of a two-dimensional (2D) heterointerface [29]. However, in many previous reports, bilayered vanadium oxides have been synthesized in the form of one-dimensional (1D) particles, such as nanowires, nanobelts, or nanorods [10, 18, 20-21, 23-26, 28-29]. The repeated intercalation/deintercalation during electrochemical cycling disturbs van der Waals bonding and/or ionic forces responsible for structural integrity, leading to electrochemical instability. Morphological stabilization has never been explored because the formation of 2D BVO was deemed too challenging if not impossible, despite the inherent 2D nature of the material structure.

The most commonly used scalable synthesis of BVOs is a sol-gel reaction between the orthorhombic α-V_2O_5 vanadium precursor and hydrogen peroxide followed by hydrothermal treatment [10, 24-26, 28]. Alternative vanadium precursors have never been explored in the H_2O_2-induced sol-gel process for the synthesis of bilayered vanadium oxides. Potential 2D precursors for BVO can be found in a diverse family of 2D transition metal carbides, nitrides, and carbonitrides, known as MXenes. They have a general structure of $M_{n+1}X_nT_x$, where M is an early transition metal (V, Nb, Mo, Ti, etc.), X is C and/or N, T_x represents the surface groups (=O, -OH, -F, -Cl), and n =1-4 [30-31]. Because MXenes have controllable interlayer spacings, they are capable of reversible intercalation of Li^+, Na^+, Mg^{2+}, and other ions [32-35]. Due to their versatile chemistry and 2D morphology, MXenes can be unique precursors for the synthesis of other classes of materials, such as oxides, metal-organic frameworks (MOFs), and composites [36-42]. In these approaches, the MXene phase serves as a transition metal precursor with the anionic sublattice being modified according to the reaction conditions. For example, $Ti_3C_2T_x$ was converted to TiS_2 by annealing in Ar/H_2S flow [43]. Oxidation, chlorination, nitridation, fluorination or sulfidation approaches were shown to be efficient preparation strategies leading to novel MXene-derived materials for energy storage applications [44].

The transformation of MXenes into oxide phases was previously conducted by a room-temperature sol-gel process or hydrothermal treatment [36-40]. It is believed that the oxygen-containing functional groups facilitate the formation of oxide phases [36]. By adding hydrogen peroxide into a $Ti_3C_2T_x$ suspension, a Ti-peroxo complex gel was created in order to prepare TiO_2/reduced graphene oxide (RGO) composites, which showed promising performance as anodes

in Na-ion capacitors [37]. When the reaction between $Ti_3C_2T_x$ MXene and H_2O_2 was carried out in alkaline solutions (NaOH or KOH), ultrathin nanoribbons of layered sodium titanate ($NaTi_{1.5}O_{8.3}$) and potassium titanate ($K_2Ti_4O_9$), respectively, were synthesized and demonstrated high performance as electrodes in Na-ion and K-ion batteries [38]. Carbon-doped TiO_2 catalysts for photocatalytic hydrogen evolution were synthesized by hydrothermal treatment of tetramethyl ammonium-intercalated $Ti_3C_2T_x$ crystals at 160 °C for 9 h [36]. Transformative oxidation approaches have been also shown efficient for MXene phases beyond $Ti_3C_2T_x$. $KNbO_3$ crystals with ferroelectric properties were fabricated from Nb_2CT_x dispersed in a KOH solution followed by hydrothermal treatment at 190 °C [39]. Molybdenum oxide/carbon composites were prepared by mild oxidation of Mo_2CT_x under CO_2 flow at 500 °C and 850 °C [40].

MXenes were also used for the fabrication of MOF structures. 2D MOF sheets and thin films were solvothermally prepared using V_2CT_x and H_2TCPP (meso-tetra(4-carboxyl-phenyl) porphyrin) ligands to produce a V-PMOF structure [41]. The evolution of the layered structure was attributed to the highly electronegative atoms on the V_2CT_x surface, facilitating bridging between the intralayer vanadium atoms and organic ligands via a deprotonation reaction. Additionally, the high MXene surface area ensures sufficiently accessible attacking sites for H_2TCPP ligands, which accelerate the reaction while preserving the 2D morphology [41]. However, to the best of our knowledge, no reports exist on conversion of V_2CT_x to 2D or layered oxides.

In this study, we demonstrate the reorganization of V_2CT_x framework via anionic sublattice modification, leading to the formation of bilayered vanadium oxides. The transformation was conducted in a two-step process with the sol-gel reaction followed by hydrothermal treatment (**Figure 1**). The oxidation transformation was accompanied by chemical preintercalation of alkali and alkaline-earth ions via the addition of inorganic chlorides into the reaction mixture, leading to the formation of δ-$M_xV_2O_5{\cdot}nH_2O$ (M = Li, Na, K, Mg, Ca) layered polymorphs with tunable interlayer distances. The V_2CT_x-derived bilayered vanadium oxides demonstrate a unique 2D morphology, which has never been previously achieved for this family of materials. Electrochemical testing of δ-$Li_xV_2O_5{\cdot}nH_2O$ and δ-$Mg_xV_2O_5{\cdot}nH_2O$ electrodes in Li-ion cells showed excellent stability in both galvanostatic cycling and rate capability experiments. We then discuss the factors that lead to the improved electrochemical performance of the MXene-derived bilayered vanadium oxide electrodes.

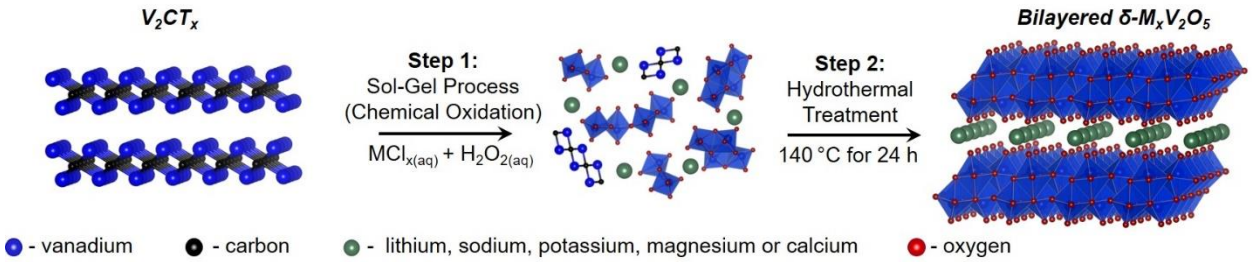

Figure 1. Schematic illustration of the two-step synthesis process, beginning with the oxidation transformation of V_2CT_x accompanied by chemical preintercalation of alkali and alkaline-earth ions, followed by hydrothermal treatment leading to the formation of δ-$M_xV_2O_5 \cdot nH_2O$ (M = Li, Na, K, Mg, Ca) layered polymorphs with tunable interlayer distance.

2. Experimental Methods

Synthesis of V_2AlC MAX Precursor

For the synthesis of MAX phase precursor, vanadium powder (99.5%, -325 mesh, Alfa Aesar), aluminum powder (99.5%, -325 mesh, Alfa Aesar), and graphite (99%, -325 mesh, Alfa Aesar), were mixed in a 2:1.1:0.9 atomic ratio. The precursors were balled milled with 10 mm zirconia balls (2:1 ball:powder ratio) in plastic jars at 50 rpm for 18 h. The powder mixture was then transferred to alumina crucibles, which were placed into a high temperature tube furnace (Carbolite Gero). Ar gas (200 cm^{-3}) was continually flown through the furnace for 1 h prior to heating and during the entire annealing procedure. The furnace was heated to 1550 °C at 3°C min^{-1}, held for 2 h, then cooled to room temperature at 3 °C min^{-1}.

Synthesis of V_2CT_x

For the topochemical synthesis of multilayered V_2CT_x, hydrochloric acid (HCl, 36.5-38%, Fisher Chemical) and hydrofluoric acid (HF, 48.5-51%, Acros Organics), were combined with deionized water at a 12:12:6 volume ratio (60 mL total). 2 g of V_2AlC powder was added to this etching solution over 5 min. The powder was stirred with a Teflon stir bar at 300 rpm at 35 °C for 120 h. After etching, the mixture was added to 150 mL polypropylene centrifugation tubes and filled with deionized water. The mixture was centrifuged at 3500 rpm for 5 minutes, and the supernatant was poured off. The sediment was re-dispersed in deionized water. This washing process was repeated until the pH was ≥ 6.

Synthesis of MXene-Derived Bilayered Vanadium Oxides

Chemically preintercalated δ-$M_xV_2O_5{\cdot}nH_2O$ (M = Li, Na, K, Mg, Ca) samples were prepared from V_2CT_x via an oxidation assisted transformation (**Figure 1**). First, 2 mL of hydrogen peroxide (30 wt.%, Fischer Scientific) was added to a mixture of 30 mL 0.5 M MCl_n solution (n = 1 and 2) and 300 mg of V_2CT_x. The reaction was conducted at room temperature under stirring at 350 rpm for approximately 2 h. Then, the resultant product, a transparent dark, green solution, was transferred into 23 mL Teflon liners (Parr Instruments Company), 15 mL of solution per liner, and autoclaved at 140 °C for 24 h. The precipitate was collected from the Teflon liners, filtered, and washed with roughly one liter of deionized water. The final product was dried at 105 °C for 12 h under ambient conditions. Thus, the synthesized MXene-derived bilayered vanadium oxides were called MD-LVO, MD-NVO, MD-KVO, MD-MVO, and MD-CVO for chemically preintercalated Li^+, Na^+, K^+, Mg^{2+}, and Ca^{2+} ions, respectively.

Materials Characterization

The analysis of the structure of δ-$M_xV_2O_5{\cdot}nH_2O$ samples was carried out using a Rigaku benchtop powder X-ray diffractometer (XRD) with Cu K_α (λ = 1.54 Å) radiation. XRD patterns were collected using a step size of 0.02° and step speed of 0.7 °·min^{-1}. The morphology of the particles was investigated using a Zeiss Supra 50VP scanning electron microscope (SEM) equipped with a Schottky field emission and Everhart-Thornley in-lens secondary electron detector. SEM images were acquired using a beam accelerating voltage of 5 kV. Additionally, samples were sputter coated with a thin ~5 nm layer of Pt/Pd to prevent surface charging and improve image quality. Elemental analysis was carried out using an equipped Oxford energy dispersive X-ray (EDX) attachment. EDX spectra were collected using a beam accelerating voltage of 20 kV and chemical compositions were estimated by averaging the EDX spectra of three separate regions (10 x 10 μm) on the samples. The water content was investigated using thermogravimetric analysis (TGA) under ambient air flow using a TA Instruments Q50 by evaluating weight loss from room temperature to 1000 °C using a heating rate of 10 °C ·min^{-1}. Raman spectra were collected from 100 to 2000 cm^{-1}, using a Renishaw inVia Raman microscope equipped with a 514 nm Ar-ion laser. X-ray photoelectron spectroscopy (XPS) measurements were recorded on a Physical Electronics VersaProbe 5000 using a monochromatic Al Kα source and charge compensation. The high-resolution V 2p spectra were taken at a pass energy of 23.5 eV

with a step size of 0.05 eV. Peak fitting and data analysis were carried out using CasaXPS software. A Shirley background was used for V 2p spectra quantification.

Electrode and Cell Fabrication

Electrodes were fabricated by dispersing the active material (70 wt. %), acetylene carbon black (20 wt. %) and poly(vinylidene fluoride) (10 wt. %) in N-methyl-2-pyrrolidone (NMP) to form a viscous slurry using a Flacktek SpeedMixer. The prepared slurry was casted onto aluminum foil and dried in an oven at 105 °C for 12 h. 10 mm electrode disks were cut from the dried films. Coin cells were assembled in an argon filled glovebox.

Electrochemical Testing

All electrochemical data were collected in 2016 type coin cells with a two-electrode format. Lithium metal foil served as both the counter and reference electrodes, polypropylene/polyethylene membrane (2325, Clegard USA) was placed in the cells as a separator, and premixed LP40 product (Gotion, 1M $LiPF_6$ in 1:1 vol/vol ethylene carbonate (EC)/diethyl carbonate (DEC)) was used as the electrolyte. All materials were tested in a voltage range of 2.0 – 4.0 V vs Li/Li^+. Cyclic voltammograms were collected using a BioLogic VP3 potentiostat at a sweep rate of 0.1 $mV \cdot s^{-1}$. Galvanostatic cycling experiments were run at a C/3 charge/discharge rate on an Arbin battery testing station. Additionally, the rate capability experiments were conducted for 5 cycles each at the follow C-rates: C/10, C/5, 1C, 5C, C/10. Finally, electrochemical impedance spectroscopy (EIS) measurements were collected using a Gamry potentiostat by applying an alternating voltage in the frequency range between 10 mHz and 200 kHz at V_{oc}, 0% state-of-charge (SOC), and 100% SOC during the 1st cycle. EIS measurements were again taken at 0% SOC and 100% SOC after 10 cycles at C/10. Here, the SOC was defined as a range between the upper and lower limits of the voltage window (100% SOC at 4.0 V and 0% SOC at 2.0 V).

3. Results and Discussion

XRD measurements, shown in **Figure 2a**, were carried out to determine the phase composition of the MXene-derived oxides. The XRD patterns of all δ-$M_xV_2O_5{\cdot}nH_2O$ (M = Li, Na, K, Mg, Ca) samples exhibit (00*l*) reflections, which are characteristic of bilayered vanadium oxide, with the (001) Bragg peak being the primary reflection. The (001) peak is located at 5-10° 2θ and corresponds to the d-spacing in structures of the synthesized materials [25, 28-29]. The primary (001) reflection and the lower intensity reflections are in agreement with previous structural analysis of δ-$V_2O_5{\cdot}nH_2O$ phase [5] and confirms that the vanadium oxide structure is likely a monoclinic unit cell (C2/m space group) comprised of bilayer stacks, which in turn are built from distorted edge sharing VO_6 octahedra. The d-spacing of MXene-derived bilayered vanadium oxides is dependent on the nature and amount of chemically preintercalated species (ions and water molecules) and ranges between 9.79 and 13.71 Å (**Figure 2a** and **Table 1**). The XRD patterns show different degrees of broadening of the (001) peak (FWHM values in **Table 1**) suggesting that the stacking of V-O layers and overall crystallinity of the materials depend on the nature of chemically preintercalated ions.

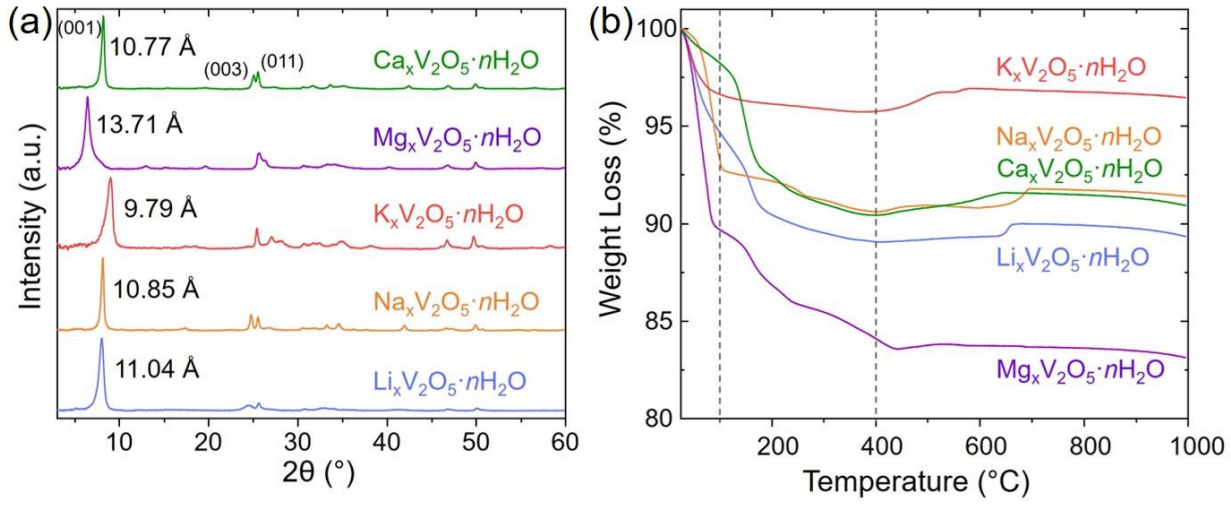

Figure 2. Structure and chemical composition of the V_2CT_x-derived δ-$M_xV_2O_5{\cdot}nH_2O$ (M = Li, Na, K, Mg, Ca) powders: (a) XRD patterns, (b) TGA weight loss curves.

Table 1. Structure and chemical composition characterization of MXene-derived bilayered vanadium oxides

M in δ-$M_xV_2O_5 \cdot nH_2O$	d-spacing, Å (XRD)	FWHM for (001) peak, ° 2θ (XRD)	M : V ratio (EDX)	x in δ-$M_xV_2O_5 \cdot nH_2O$	*n* in δ-$M_xV_2O_5 \cdot nH_2O$ (TGA)
Li	11.04	0.61	-	-	0.60
Na	10.85	0.33	0.17	0.34	0.27
K	9.79	0.81	0.22	0.44	0.09
Mg	13.71	0.38	0.08	0.16	0.66
Ca	10.77	0.62	0.11	0.22	0.86

Previously reported bilayered vanadium oxides, prepared using chemical preintercalation synthesis with α-V_2O_5 as the precursor, demonstrated a direct correlation between the d-spacing and hydrated interlayer ion radius [26]. Li-, Na-, K-, and Mg-preintercalated MXene-derived oxides, synthesized in this work, follow the same trend: the d-spacing increases with an increase of the hydrated preintercalated ions radii (**Table 1** and **Table S1** in Supporting Information). However, the d-spacing of MD-CVO phase (10.77 Å) is significantly smaller than that reported for Ca-preintercalated δ-V_2O_5 obtained from the α-V_2O_5 precursor (12.44 Å) [26] and does not follow the general trend. The XRD pattern of MD-CVO is in good agreement with a calcium-vanadium-bronze phase crystallized in a monoclinic space group C2/m (a = 11.805, b = 3.709, c = 9.270, β = 101.87°), where Ca^{2+} cations are statistically distributed in two independent crystallographic positions [45].

The d-spacing in hydrated complex layered compounds depends on both the nature and amount of interlayer ions and structural water content. To determine the hydration degree of the MXene-derived bilayered vanadium oxides (i.e. *n* in δ-$M_xV_2O_5 \cdot nH_2O$), we analyzed TGA weight loss curves from 25 – 1000 °C (**Figure 2b**). Generally, the weight loss observed below 100 °C is attributed to the evaporation of weakly bound water on the surface of the materials. To assess the interlayer water content, the weight loss from approximately 100 – 400 °C (440 °C in case of δ-$Mg_xV_2O_5 \cdot nH_2O$) was used. A summary of the hydration degrees is shown in **Table 1**. The d-spacing increases with the increase of interlayer water content for all materials, except for MD-CVO. The hydrated ion radius is estimated assuming octahedral water coordination (**Table S1,** Supporting Information). However, previous calculation of Mg^{2+} and Ca^{2+} hydration properties revealed that while Mg^{2+} is at the global free-energy minimum for six-fold coordination, the hydrated Ca^{2+} free-energy curve shows several shallow local minima, suggesting that the hydration

structure of Ca^{2+} ion is variable [46]. Therefore, it is possible that interlayer Ca^{2+} ions and water molecules form clusters with different geometries contrary to the interlayer region of δ-$M_xV_2O_5{\cdot}nH_2O$ (M = Li, Na, K, Mg), causing δ-$Ca_xV_2O_5{\cdot}nH_2O$ to be the exception from the observed trend. A weight gain observed above ~450 °C may occur due to the filling of oxygen vacancies in V-O layers [47]. Similar thermogravimetric behavior has been reported for bilayered vanadium oxides synthesized from α-V_2O_5 precursor [28].

To better understand the transformation of V_2CT_x into bilayered vanadium oxides, it is important to discern the destiny of the carbon in the initial MXene structure. To answer this question, Raman spectra were collected between 100 – 2000 cm^{-1} (**Figure 3**). The absence of bands in the double bond region (i.e. -C=O, -C=C-; 1600-1800 cm^{-1}), which are characteristic of the carbon within MXenes [48], confirms that the transformation was completed. Additionally, for all V_2CT_x-derived δ-$M_xV_2O_5{\cdot}nH_2O$ samples, there are no D and G spectral bands present in the 1100-1800 cm^{-1} Raman shift region indicating an absence of any bonded or disordered carbon. A previous report showed that heating $Ti_3C_2T_x$ in air yields nanocrystalline anatase TiO_2 formed on the surface of disordered graphitic carbon sheets, confirmed by the presence of D and G bands [49]. Here instead, a possible mechanism (**Equation 1**) occurs where CO/CO_2 gas is formed during the transformation and emitted from the reaction vessel, similar to a previous study on the chemical oxidation of Ti_2CT_x [50]. This is consistent with the observed formation and emission of gas during synthesis for all V_2CT_x-derived δ-$M_xV_2O_5{\cdot}nH_2O$ samples.

$$V_2C + xM^{z+}_{(aq)} + 6H_2O_2 \rightarrow M_xV_2O_5 + CO_{y(g)} \uparrow + 6H_2O \qquad (1)$$

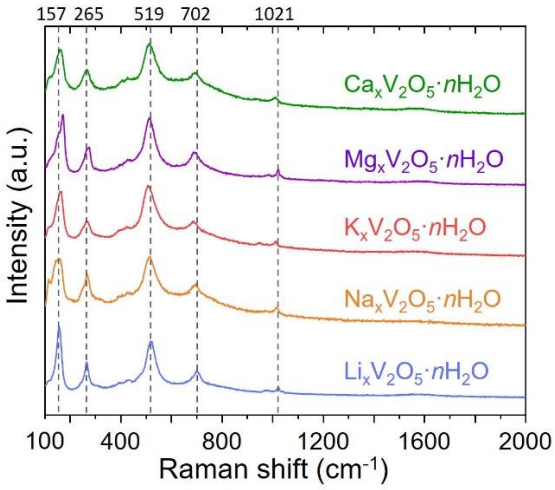

Figure 3. Raman spectra of V_2CT_x-derived δ-$M_xV_2O_5 \cdot nH_2O$ (M = Li, Na, K, Mg, Ca) powders

The Raman spectra from 100 - 1100 cm^{-1} contain bands associated with the fingerprints of the bilayered vanadium oxide framework, where the spectral bands are characteristic of the backbone of the material. Generally, V_2CT_x-derived δ-$M_xV_2O_5 \cdot nH_2O$ samples exhibit similar spectra. The prevalent low wavenumber band at 157 cm^{-1} is assigned to the skeletal bent vibration of the structural framework and is characteristic of the layered δ-V_2O_5 structure [21]. The spectral bands observed at 265 cm^{-1} are attributed to the bending vibrations of the O–V–O bond [51-52]. Additionally, the spectral bands at approximately 519 and 702 cm^{-1} are associated with the bending and stretching vibrations of the V–O bond, respectively [51-52]. Lastly, the bands observed at 1021 cm^{-1} are attributed to the vanadyl mode corresponding to the stretching of the V=O bond [51, 53-54]. The skeletal bent vibration mode around 157 cm^{-1} together with the vanadyl mode at 1021 cm^{-1} are indicative of the layered δ-V_2O_5 structure [21]. Notably, the most intense band at 157 cm^{-1} in the Raman spectrum of δ-$Li_xV_2O_5 \cdot nH_2O$ sample, exhibits a decreased intensity and appears at higher Raman shift values compared to the other δ-$M_xV_2O_5 \cdot nH_2O$ samples. This could be attributed to the significant differences in d-spacing of the (001) plane (9.79 – 13.71 Å) leading to varying levels of structure distortion and bond strengths. The Raman spectra in tandem with the powder XRD data confirm the distorted bilayered structure of δ-$M_xV_2O_5 \cdot nH_2O$.

Figure 4 shows SEM images of the V_2CT_x-derived δ-$M_xV_2O_5 \cdot nH_2O$ powders synthesized in this work. Strikingly, all five phases crystallized as 2D sheets, which has never been reported for bilayered vanadium oxides synthesized from α-V_2O_5-based sol-gels. Past reports demonstrated

1D nanobelt or nanowire particles [24-26, 28]. In this study, MD-LVO formed flexible nanoflakes stacked into a film-like architecture with some pores between the flakes (**Figure 4a, b**). Na-, K-, Mg- and Ca-preintercalated δ-$V_2O_5 \cdot nH_2O$ phases showed a flower-like morphology comprised of 2D nanoplatelets growing outward from the center of the flower (**Figure 4, c-j**). In case of MD-NVO and MD-KVO, the nanoplatelets are mostly straight, while MD-MVO and MD-CVO twist and form more intricate agglomerates. Analysis of the high magnification SEM images (**Figure 4b, d, f, h, i**) revealed that some nanoplatelets were composed of co-aligned nanobelts intergrown together. The lateral dimension of the nanoplatelets ranges from a few to 10 μm. The unique morphology of V_2CT_x-derived δ-$M_xV_2O_5 \cdot nH_2O$ nanoparticles may stem from the 2D nature of the V_2CT_x precursor. The oxidized sol particles formed during the reaction between V_2CT_x and H_2O_2 are likely to maintain a 2D shape, thus forcing condensation on the edges of such a nucleus. Since no capping agents were used in our synthesis protocol, multiple 2D nuclei could agglomerate giving rise to a flower-like morphology observed for most V_2CT_x-derived bilayered vanadium oxides.

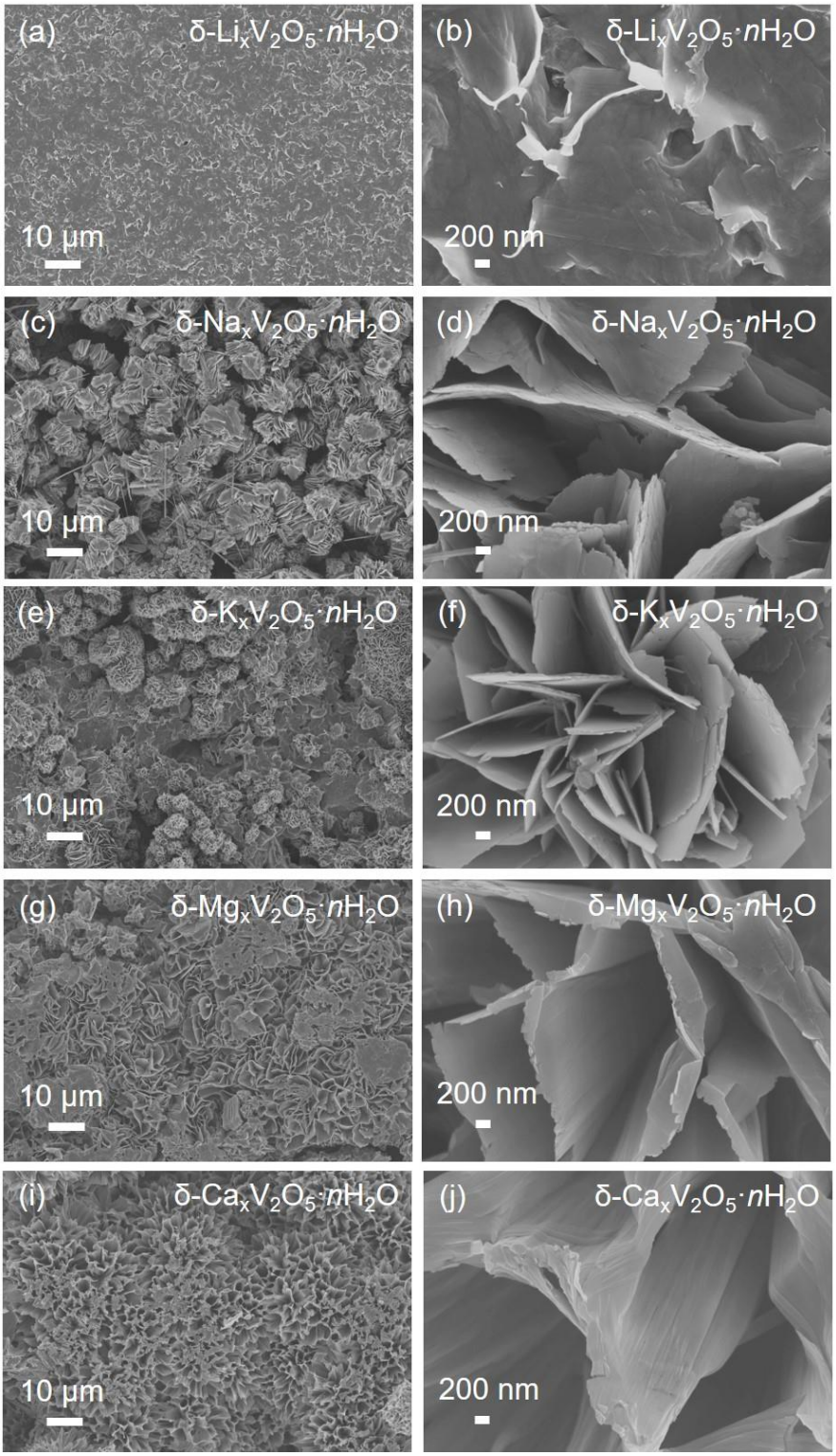

Figure 4. SEM images of the V_2CT_x-derived (a, b) δ-$Li_xV_2O_5{\cdot}nH_2O$, (c, d) δ-$Na_xV_2O_5{\cdot}nH_2O$, (e, f) δ-$K_xV_2O_5{\cdot}nH_2O$, (g, h) δ-$Mg_xV_2O_5{\cdot}nH_2O$ and (i, j) δ-$Ca_xV_2O_5{\cdot}nH_2O$ samples. (a, c, e, g, i) Low and (b, d, f, h, j) high magnification images are shown.

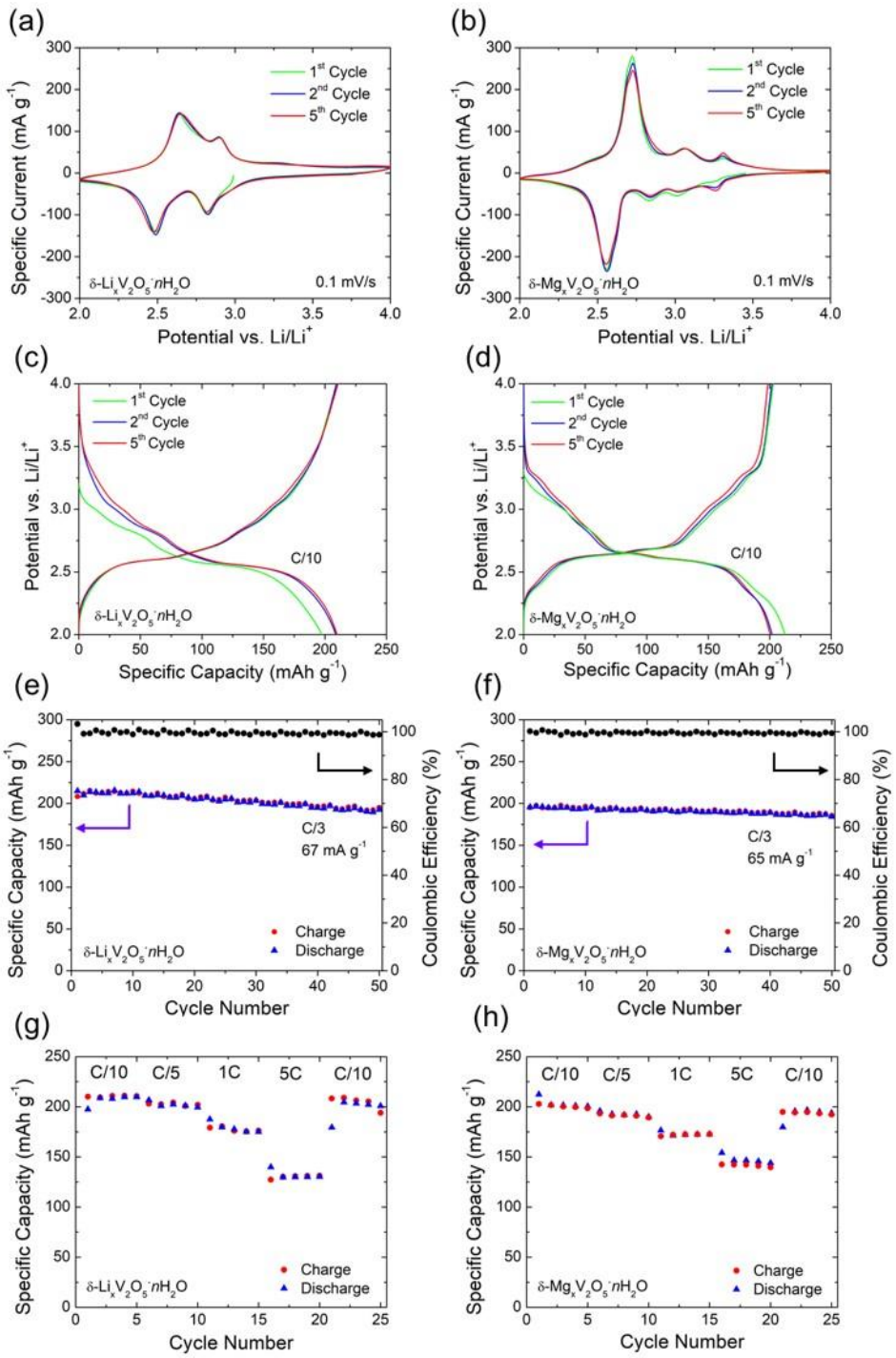

Figure 5. Electrochemical characterization of the V_2CT_x-derived (a, c, e, g) δ-$Li_xV_2O_5{\cdot}nH_2O$ and (b, d, f, h) δ-$Mg_xV_2O_5{\cdot}nH_2O$ electrodes in Li-ion half-cells. (a, b) Cyclic voltammograms collected at a scan rate of 0.1 $mV{\cdot}s^{-1}$. (c, d) 1st, 2nd and 5th cycle galvanostatic discharge/charge profiles at a current rate of C/3. (e, f) Extended cycling and coulombic efficiency of both electrodes cycled at current rate of C/3. (g, h) Rate performance of both electrodes consisting of 5 cycles at each of the following current rates: C/10, C/5, 1C, 5C and C/10.

The electrochemical performance of V_2CT_x-derived δ-$M_xV_2O_5{\cdot}nH_2O$ electrodes was evaluated in Li-ion half-cells. Galvanostatic discharge/charge cycling for 50 cycles revealed that Li- and Mg-preintercalated bilayered vanadium oxides demonstrated the highest stability (**Figure S1**, Supporting Information). Interestingly, when used as a cathode in Li-ion cells, MD-LVO represents a material that is chemically preintercalated with electrochemically cycled ions. Previous reports indicated that in these cases, facilitated diffusion is achieved due to the synthetically-controlled formation of intercalation sites well-defined for the insertion and movement of electrochemically cycled ions [25]. MD-MVO, on the other hand, represents a pillared layered phase in which chemically preintercalated ions (Mg^{2+} ions) and electrochemically cycled ions (Li^+ ions in Li-ion cells) are different. Moreover, in case of the bilayered vanadium oxides obtained from α-V_2O_5-based sol-gels, δ-$Mg_xV_2O_5{\cdot}nH_2O$ electrode showed the highest initial capacity, greatest capacity retention, and highest rate capability of all five materials [26]. Therefore, MD-LVO and MD-MVO phases have been selected for a more detailed electrochemical study.

Figure 5 shows the electrochemical performance of V_2CT_x-derived δ-$Li_xV_2O_5{\cdot}nH_2O$ and δ-$Mg_xV_2O_5{\cdot}nH_2O$ electrodes in Li-ion cells. The CV curve of the MD-LVO exhibits two reversible and broad cathodic peaks at 2.85 and 2.50 V vs Li/Li^+. The corresponding anodic peaks appear at 2.60 and 2.90 V. The shape of the CV curve of the MD-MVO electrode is distinctly different with a prominent single pair of cathodic and anodic peaks at 2.75 and 2.55 V, respectively, and several peaks with lower intensities at ~2.80 – 3.40 V. These peaks are indicative of reversible ion intercalation type behavior. The small difference (< 300 mV) between the corresponding cathodic and anodic peak voltages suggests high reversibility of ion intercalation and deintercalation leading to low overpotential. However, the difference in the shape of CV curves implies that the crystallographic sites for Li^+ ion intercalation in MD-LVO and MD-MVO phases are different. In fact, electrochemically cycled Li^+ ions in the interlayer spacing of MD-LVO can move through the positions defined by chemically preintercalated Li^+ ions. While, for MD-MVO, the electrochemically cycled Li^+ ions might require pathways to bypass chemically preintercalated pillaring Mg^{2+} ions to move within the interlayer region. The cathodic peak at ~2.50 V present in the CV curves of both materials could correspond to the diffusion of electrochemically cycled Li^+ ions around chemically preintercalated ions. While the prominent reversible cathodic peak at ~2.85 V, which only appears for MD-LVO, could be attributed to the replacement diffusion mechanism, whereby electrochemically cycled Li^+ ions replace chemically preintercalated Li^+ ions by pushing

them further inside the 2D structural tunnel. Despite the similar electrochemical charge storage behavior of the δ-$M_xV_2O_5{\cdot}nH_2O$ (M = Li, Na, K, Mg, Ca), our results indicate that the electrodes could be substantially different and depend on the nature of chemically preintercalated ion. More detailed *-in-situ* studies are needed to completely understand the diffusion of Li^+ ions in the interlayer region and differences between these materials.

The galvanostatic discharge/charge curves for the 1st, 2nd and 5th cycles of MD-LVO and MD-MVO electrodes at a current rate of C/10 are shown in **Figure 5c** and **5d**, respectively. The initial cycling revealed that MD-LVO delivered a reversible specific capacity of 210 $mAh{\cdot}g^{-1}$ (**Figure 5c**), while the specific capacity of the MD-MVO decreases from 212 $mAh{\cdot}g^{-1}$ in the 1st cycle and stabilizes at ~198 $mAh{\cdot}g^{-1}$ (**Figure 5d**). The specific capacities at relatively low cycling rates were used to calculate C-rates for the following extended galvanostatic cycling and rate capability experiments. To further understand the specific capacity values shown by MD-LVO and MD-MVO, XPS measurements were carried out to determine the oxidation state of vanadium in pristine electrodes (**Figure 6**). Analysis of the V 2p spectra revealed that the vanadium is present in a mixed V^{5+}/V^{4+} oxidation state. The fraction of V^{5+} is approximately 84% for both MD-LVO and MD-MVO. This value is in excellent agreement with the formula for V_2CT_x-derived Mg-preintercalated bilayered vanadium oxide, δ-$Mg_{0.16}V_2O_5{\cdot}0.66H_2O$ (**Table 1**), estimated via EDX analysis. Interestingly, MD-LVO and MD-MVO phases have the lowest fraction of V^{4+} ions, (**Figure S2** in Supporting Information) which could be related to the highest electrochemical performance exhibited by these two materials. Partial reduction of vanadium occurs due to the introduction of the chemically preintercalated ions into the interlayer regions. However, the large fraction of V^{5+} indicates high redox activity and agrees with high values of the observed specific capacities. The specific capacity of 193 $mAh{\cdot}g^{-1}$ delivered by the δ-$Mg_xV_2O_5{\cdot}nH_2O$ electrode corresponds to a ~1.4 electron process and can be described by the following equation:

$$Mg_{0.16}V_2O_5 \cdot 0.66H_2O + 1.4e^- + 1.4Li^+ \rightarrow Li_{1.4}Mg_{0.16}V_2O_5 \cdot 0.66H_2O \qquad (2)$$

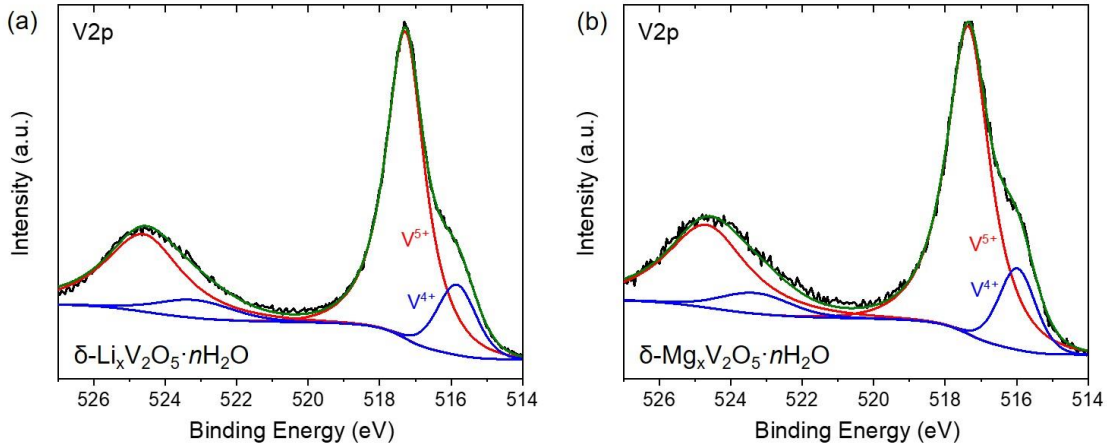

Figure 6. XPS spectra of the V2p region for the V_2CT_x-derived (a) δ-$Li_xV_2O_5{\cdot}nH_2O$ and (b) δ-$Mg_xV_2O_5{\cdot}nH_2O$ materials.

The electrochemical stability of the MD-LVO and MD-MVO electrodes was accessed by cycling at a current rate of C/3 for 50 cycles (**Figure 4e** and **4f**, respectively). Both phases exhibited good cycling stability with coulombic efficiencies of ~99-100% in all Li^+ intercalation/ deintercalation cycles. After 50 cycles, the MD-LVO electrode demonstrated a specific discharge capacity of 193 $mAh{\cdot}g^{-1}$ with capacity retention of 90%. The MD-MVO electrode demonstrated a specific discharge capacity of 184 $mAh{\cdot}g^{-1}$ with a capacity retention of 94% after 50 cycles. Interestingly, the best performing bilayered vanadium oxide synthesized from α-V_2O_5 showed a capacity retention of only 81.8% after cycling for 50 cycles at a current density of 20 $mA{\cdot}g^{-1}$ [26]. Typically, the δ-$(M_x)V_2O_5{\cdot}nH_2O$ phases synthesized via sol-gel approaches exhibit severe capacity fading upon extended cycling which is largely attributed to the loss of the lamellar order of the V-O layers [9]. Here, the improved capacity retention may be attributed to the improved stacking of the V-O layers owed to the novel synthesis route possibly leading to the morphological stabilization of the material structure during extended cycling.

The tolerance of the MD-LVO and MD-MVO phases to high currents, which is important for fast charging, was tested by cycling at a constant symmetrical current rate for five cycles and then increasing the current rate stepwise. The drops in specific discharge capacity with increasing current rate were evaluated. To understand the stability and recovery of the electrodes, the current rate was brought back to the lowest value after cycling for five cycles at the highest current rate. The selected current rates were C/10, C/5, 1C, 5C before returning to C/10 (**Figure 5g** and **5h**). Both materials showed excellent rate capability and tolerance to high C-rates. MD-LVO electrode

exhibited a specific discharge capacity of 130 mAh·g^{-1} at a current rate of 5C. More impressively, the MD-MVO electrode demonstrated a specific discharge capacity of ~146 mAh·g^{-1} at the 5C current rate. The higher discharge capacity at the highest current rate of MD-MVO electrodes may be attributed to the elaborate flower-like surface morphology of the Mg-preintercalated phase, which enables higher contact area with electrolyte compared to the MD-LVO particles (**Figure 4**). For both materials, the capacity recovered when the current rate was returned back to the value of C/10 after cycling at 5C-rate, suggesting that no significant damage to the structure of MD-LVO and MD-MVO phases occurred at high currents.

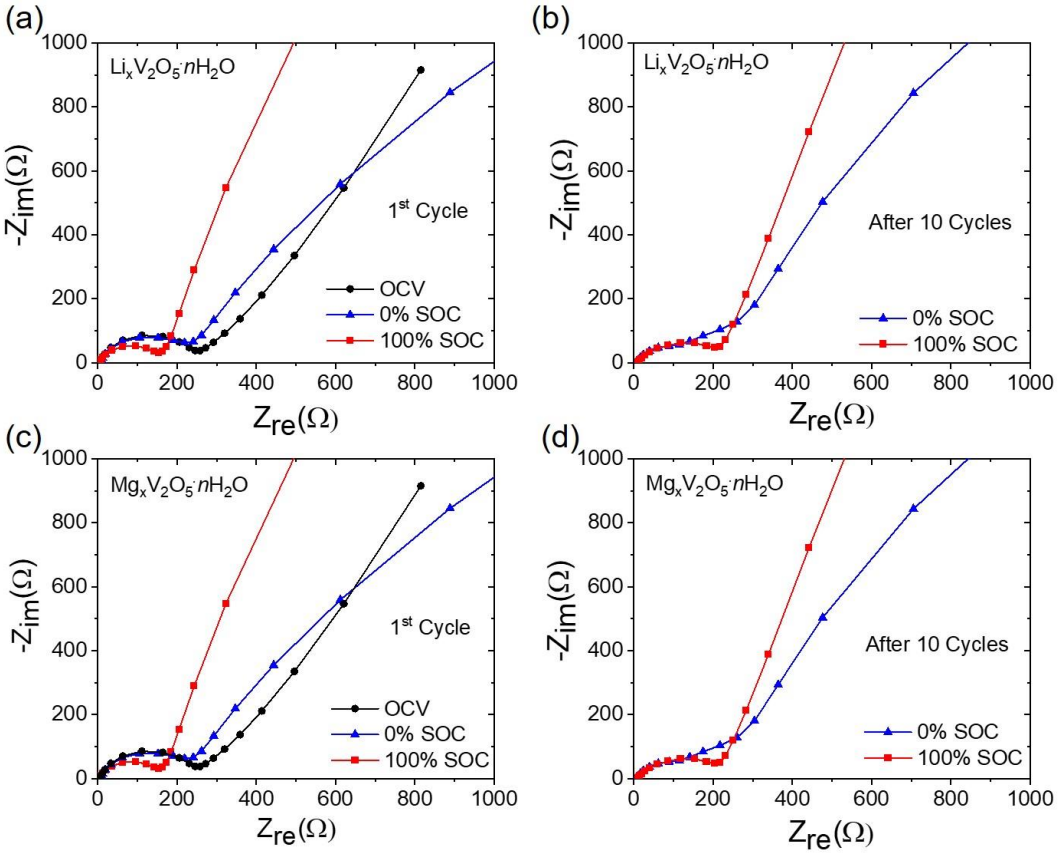

Figure 7. EIS data of the Li-ion cells containing V_2CT_x-derived (a, b) δ-$Li_xV_2O_5{\cdot}nH_2O$ and (c, d) δ-$Mg_xV_2O_5{\cdot}nH_2O$ electrodes in (a, c) the 1st electrochemical cycle and (b, d) after 10 electrochemical cycles at a current rate of C/10. The EIS spectra were collected during the 1st cycle at OCV, 0% SOC and 100% SOC; and after 10 cycles at 0% and 100% SOC.

To understand the reasons for the capacity decay observed in both galvanostatic extended cycling and rate capability experiments, the charge/discharge behavior of the MD-LVO and MD-MVO electrodes was analyzed using electrochemical impedance spectroscopy (EIS). **Figure 7**

shows the Nyquist plots obtained in the first Li^+ ion intercalation/deintercalation cycle and after 10 electrochemical cycles. All of the impedance spectra have similar shapes: a medium-to-high frequency depressed semicircle corresponding to the solution and interfacial charge transfer impedance, and an inclined low-frequency tail attributed to the lithium diffusion impedance. EIS studies showed that the interfacial charge transfer resistance increases with cycling which could be due to the formation of poorly conducting solid-electrolyte interface (SEI) layer. The growing SEI layer could contribute to the observed slow loss of capacity during cycling. Still, the V_2CT_x-derived bilayered vanadium oxide electrodes with 2D morphology demonstrated record stability in Li-ion cells compared to δ-$M_xV_2O_5{\cdot}nH_2O$ phases synthesized via sol-gel process-based methods starting from alternative vanadium precursors.

4. Conclusions

In this study, we have developed a new synthesis route for preparation of δ-$M_xV_2O_5{\cdot}nH_2O$ with enhanced properties. This approach uses a H_2O_2-assisted MXene oxidation method consisting of a sol-gel process in the presence of alkali and alkaline-earth metal chlorides followed by hydrothermal treatment of the resulting peroxo vanadium gel for the synthesis of chemically preintercalated bilayered vanadium oxides with tunable d-spacing. By utilizing V_2CT_x as the vanadium precursor, the synthesis time was shortened because an extended aging step was not needed, and the energy consumption was reduced by lowering the hydrothermal treatment temperature from 220 °C to 140 °C compared to approaches using α-V_2O_5 [24-26, 28-29]. V_2CT_x-derived δ-$M_xV_2O_5{\cdot}nH_2O$ (M = Li, Na, K, Mg, Ca) phases demonstrated a unique 2D flower-like morphology, possibly resulting from the 2D nature of the V_2CT_x MXene precursor. Raman spectroscopy analysis showed absence of carbon bands, indicating that the MXene-to-oxide transformation was accompanied by formation of volatile carbon-based compounds.

The V_2CT_x-derived δ-$M_xV_2O_5{\cdot}nH_2O$ (M = Li, Na, K, Mg, Ca) electrodes demonstrated high initial specific capacities in Li-ion cells, while Li- and Mg-preintercalated bilayered vanadium oxides showed initial specific discharge capacities of 200 $mAh{\cdot}g^{-1}$ and 192 $mAh{\cdot}g^{-1}$, respectively, and excellent electrochemical stability during extended cycling with 89% and 94% capacity retention after 50 cycles when cycled at a C/3 rate (178 $mAh{\cdot}g^{-1}$ and 180 $mAh{\cdot}g^{-1}$, respectively). Impressively, V_2CT_x-derived δ-$Li_xV_2O_5{\cdot}nH_2O$ and δ-$Mg_xV_2O_5{\cdot}nH_2O$ electrodes demonstrated exceptional tolerance to high current rates and specific discharge capacities of 130 $mAh{\cdot}g^{-1}$ and

146 mAh·g^{-1} at a current rate of 5C, respectively. The advanced electrochemical properties are attributed to 2D morphology of V_2CT_x-derived bilayered vanadium oxides combined with the structure and composition of the synthesized materials. While this study focused on bilayered vanadium oxides, this synthesis route can be used with other MXenes enabling the production of oxides with different chemistries or mixed oxides. Furthermore, it is possible for new metastable phases with enhanced functionalities that cannot be synthesized using traditional routes to be produced by utilizing MXenes as precursors.

Supporting Information

Table containing the size of chemically preintercalated ions in the ionic and hydrated ion forms; 1^{st}, 2^{nd}, 10^{th}, 20^{th} and 50^{th} discharge/charge curves of the Li-ion cell containing MXene-derived δ-$M_xV_2O_5{\cdot}nH_2O$ (M = Li, Na, K, Mg, Ca) electrodes at a current rate of C/3; and XPS spectra of the V 2p core level for δ-$M_xV_2O_5{\cdot}nH_2O$ (M = Li, Na, K, Mg, Ca) powders.

Acknowledgements

This work was supported by the National Science Foundation Grant Nos. DMR-1752623 and DMR-1609272. We acknowledge Drexel's Centralized Research Facilities for help with materials characterization. Development of MXene at Drexel University by Y.G. was supported in part by Murata Manufacturing Co., Ltd.

References

1. Pomerantseva, E.; Bonaccorso, F.; Feng, X.; Cui, Y.; Gogotsi, Y., Energy storage: The future enabled by nanomaterials. *Science* **2019,** *366* (6468), eaan8285.
2. Liu, J. H.; Liu, X. W., Two-Dimensional Nanoarchitectures for Lithium Storage. *Advanced Materials* **2012,** *24* (30), 4097-4111.
3. Rozier, P.; Tarascon, J. M., Review-Li-Rich Layered Oxide Cathodes for Next-Generation Li-Ion Batteries: Chances and Challenges. *Journal of the Electrochemical Society* **2015,** *162* (14), A2490-A2499.
4. Xu, J.; Lin, F.; Doeff, M. M.; Tong, W., A review of Ni-based layered oxides for rechargeable Li-ion batteries. *Journal of Materials Chemistry A* **2017,** *5* (3), 874-901.
5. Petkov, V.; Trikalitis, P. N.; Bozin, E. S.; Billinge, S. J. L.; Vogt, T.; Kanatzidis, M. G., Structure of $V_2O_5{\cdot}nH_2O$ Xerogel Solved by the Atomic Pair Distribution Function Technique. *Journal of the American Chemical Society* **2002,** *124* (34), 10157-10162.
6. Moretti, A.; Passerini, S., Bilayered Nanostructured $V_2O_5{\cdot}nH_2O$ for Metal Batteries. *Advanced Energy Materials* **2016,** *6* (23).
7. Clites, M.; Byles, B. W.; Pomerantseva, E., Bilayered Vanadium Oxide as the Host Material for Reversible Beyond Lithium Ion Intercalation *Advanced Materials Letters* **2017,** *8* (6), 679-688.
8. Tepavcevic, S.; Liu, Y.; Zhou, D.; Lai, B.; Maser, J.; Zuo, X.; Chan, H.; Král, P.; Johnson, C. S.; Stamenkovic, V.; Markovic, N. M.; Rajh, T., Nanostructured Layered Cathode for Rechargeable Mg-Ion Batteries. *ACS Nano* **2015,** *9* (8), 8194-8205.
9. Tepavcevic, S.; Xiong, H.; Stamenkovic, V. R.; Zuo, X.; Balasubramanian, M.; Prakapenka, V. B.; Johnson, C. S.; Rajh, T., Nanostructured Bilayered Vanadium Oxide Electrodes for Rechargeable Sodium-Ion Batteries. *ACS Nano* **2012,** *6* (1), 530-538.
10. Moretti, A.; Giuli, G.; Trapananti, A.; Passerini, S., Electrochemical and structural investigation of transition metal doped V_2O_5 sono-aerogel cathodes for lithium metal batteries. *Solid State Ionics* **2018,** *319*, 46-52.
11. Moretti, A.; Maroni, F.; Osada, I.; Nobili, F.; Passerini, S., V_2O_5 Aerogel as a Versatile Cathode Material for Lithium and Sodium Batteries. *ChemElectroChem* **2015,** *2* (4), 529-537.
12. Moretti, A.; Secchiaroli, M.; Buchholz, D.; Giuli, G.; Marassi, R.; Passerini, S., Exploring the Low Voltage Behavior of V_2O_5 Aerogel as Intercalation Host for Sodium Ion Battery. *Journal of The Electrochemical Society* **2015,** *162* (14), A2723-A2728.
13. Liu, X.; Elia, G. A.; Gao, X. P.; Qin, B. S.; Zhang, H.; Passerini, S., Highly Concentrated KTFSI : Glyme Electrolytes for K/Bilayered-V_2O_5 Batteries. *Batteries & Supercaps* **2020,** *3* (3), 261-267.
14. Liu, X.; Qin, B. S.; Zhang, H.; Moretti, A.; Passerini, S., Glyme-Based Electrolyte for Na/Bilayered-V_2O_5 Batteries. *Acs Applied Energy Materials* **2019,** *2* (4), 2786-2793.
15. Wei, Q.; Liu, J.; Feng, W.; Sheng, J.; Tian, X.; He, L.; An, Q.; Mai, L., Hydrated vanadium pentoxide with superior sodium storage capacity. *Journal of Materials Chemistry A* **2015,** *3* (15), 8070-8075.
16. Xu, X. M.; Duan, M. Y.; Yue, Y. F.; Li, Q.; Zhang, X.; Wu, L.; Wu, P. J.; Song, B.; Mai, L. Q., Bilayered $Mg_{0.25}V_2O_5{\cdot}H_2O$ as a Stable Cathode for Rechargeable Ca-Ion Batteries. *Acs Energy Letters* **2019,** *4* (6), 1328-1335.
17. Lee, S. H.; DiLeo, R. A.; Marschilok, A. C.; Takeuchi, K. J.; Takeuchi, E. S., Sol Gel Based Synthesis and Electrochemistry of Magnesium Vanadium Oxide: A Promising Cathode Material for Secondary Magnesium Ion Batteries. *ECS Electrochemistry Letters* **2014,** *3* (8), A87-A90.
18. Baddour-Hadjean, R.; Huynh, L. N. T.; Batyrbekuly, D.; Bach, S.; Pereira-Ramos, J. P., Bilayered Potassium Vanadate $K_{0.5}V_2O_5$ as Superior Cathode Material for Na-Ion Batteries. *Chemsuschem* **2019,** *12*, 5192-5198.
19. Brown, E.; Acharya, J.; Elangovan, A.; Pandey, G. P.; Wu, J.; Li, J., Disordered Bilayered $V_2O_5{\cdot}nH_2O$ Shells Deposited on Vertically Aligned Carbon Nanofiber Arrays as Stable High-Capacity Sodium Ion Battery Cathodes. *Energy Technology* **2018,** *6* (12), 2438-2449.

20. Kundu, D.; Adams, B. D.; Duffort, V.; Vajargah, S. H.; Nazar, L. F., A high-capacity and long-life aqueous rechargeable zinc battery using a metal oxide intercalation cathode. *Nature Energy* **2016,** *1*.
21. Su, D.; Wang, G., Single-Crystalline Bilayered V_2O_5 Nanobelts for High-Capacity Sodium-Ion Batteries. *ACS Nano* **2013,** *7* (12), 11218-11226.
22. Xu, G. B.; Liu, X.; Huang, S. J.; Li, L.; Wei, X. L.; Cao, J. X.; Yang, L. W.; Chu, P. K., Freestanding, Hierarchical, and Porous Bilayered $Na_xV_2O_5{\cdot}nH_2O$/rGO/CNT Composites as High-Performance Cathode Materials for Nonaqueous K-Ion Batteries and Aqueous Zinc-Ion Batteries. *Acs Applied Materials & Interfaces* **2020,** *12* (1), 706-716.
23. Yang, G. Z.; Wei, T. Y.; Wang, C. X., Self-Healing Lamellar Structure Boosts Highly Stable Zinc-Storage Property of Bilayered Vanadium Oxides. *Acs Applied Materials & Interfaces* **2018,** *10* (41), 35079-35089.
24. Clites, M.; Byles, B. W.; Pomerantseva, E., Effect of aging and hydrothermal treatment on electrochemical performance of chemically pre-intercalated Na-V-O nanowires for Na-ion batteries. *Journal of Materials Chemistry A* **2016,** *4* (20), 7754-7761.
25. Clites, M.; Hart, J. L.; Taheri, M. L.; Pomerantseva, E., Chemically Preintercalated Bilayered $K_xV_2O_5{\cdot}nH_2O$ Nanobelts as a High-Performing Cathode Material for K-Ion Batteries. *ACS Energy Letters* **2018,** *3* (3), 562-567.
26. Clites, M.; Pomerantseva, E., Bilayered vanadium oxides by chemical pre-intercalation of alkali and alkali-earth ions as battery electrodes. *Energy Storage Materials* **2018,** *11* (Supplement C), 30-37.
27. Liu, X. L.; Depaifve, S.; Leyssens, T.; Hermans, S.; Vlad, A., Versatile Synthesis of Vanadium(III, IV, V) Oxides@Reduced Graphene Oxide Nanocomposites and Evaluation of their Lithium and Sodium Storage Performances. *Batteries & Supercaps* **2019,** *2* (12), 1016-1025.
28. Clites, M.; Hart, J. L.; Taheri, M. L.; Pomerantseva, E., Annealing-Assisted Enhancement of Electrochemical Stability of Na-Preintercalated Bilayered Vanadium Oxide Electrodes in Na-Ion Batteries. *ACS Applied Energy Materials* **2020,** *3* (1), 1063-1075.
29. Clites, M.; Andris, R.; Cullen, D. A.; More, K. L.; Pomerantseva, E., Improving Electronic Conductivity of Layered Oxides through the Formation of Two-Dimensional Heterointerface for Intercalation Batteries. *ACS Applied Energy Materials* **2020,** *3* (4), 3835-3844.
30. Naguib, M.; Kurtoglu, M.; Presser, V.; Lu, J.; Niu, J.; Heon, M.; Hultman, L.; Gogotsi, Y.; Barsoum, M. W., Two-Dimensional Nanocrystals Produced by Exfoliation of Ti_3AlC_2. *Advanced Materials* **2011,** *23* (37), 4248-4253.
31. Deysher, G.; Shuck, C. E.; Hantanasirisakul, K.; Frey, N. C.; Foucher, A. C.; Maleski, K.; Sarycheva, A.; Shenoy, V. B.; Stach, E. A.; Anasori, B.; Gogotsi, Y., Synthesis of Mo_4VAlC_4 MAX Phase and Two-Dimensional Mo4VC4 MXene with Five Atomic Layers of Transition Metals. *ACS Nano* **2020,** *14* (1), 204-217.
32. Lukatskaya, M. R.; Mashtalir, O.; Ren, C. E.; Dall'Agnese, Y.; Rozier, P.; Taberna, P. L.; Naguib, M.; Simon, P.; Barsoum, M. W.; Gogotsi, Y., Cation Intercalation and High Volumetric Capacitance of Two-Dimensional Titanium Carbide. *Science* **2013,** *341* (6153), 1502-1505.
33. Ghidiu, M.; Halim, J.; Kota, S.; Bish, D.; Gogotsi, Y.; Barsoum, M. W., Ion-Exchange and Cation Solvation Reactions in Ti_3C_2 MXene. *Chemistry of Materials* **2016,** *28* (10), 3507-3514.
34. Kajiyama, S.; Szabova, L.; Sodeyama, K.; Iinuma, H.; Morita, R.; Gotoh, K.; Tateyama, Y.; Okubo, M.; Yamada, A., Sodium-Ion Intercalation Mechanism in MXene Nanosheets. *ACS Nano* **2016,** *10* (3), 3334-3341.
35. Bao, W.; Shuck, C. E.; Zhang, W.; Guo, X.; Gogotsi, Y.; Wang, G., Boosting Performance of Na–S Batteries Using Sulfur-Doped $Ti_3C_2T_x$ MXene Nanosheets with a Strong Affinity to Sodium Polysulfides. *ACS Nano* **2019,** *13* (10), 11500-11509.
36. Jia, G.; Wang, Y.; Cui, X.; Zheng, W., Highly Carbon-Doped TiO_2 Derived from MXene Boosting the Photocatalytic Hydrogen Evolution. *ACS Sustainable Chemistry & Engineering* **2018,** *6* (10), 13480-13486.

37. Wang, R.; Wang, S.; Zhang, Y.; Jin, D.; Tao, X.; Zhang, L., Graphene-coupled Ti_3C_2 MXenes-derived TiO_2 mesostructure: promising sodium-ion capacitor anode with fast ion storage and long-term cycling. *Journal of Materials Chemistry A* **2018,** *6* (3), 1017-1027.
38. Dong, Y.; Wu, Z.-S.; Zheng, S.; Wang, X.; Qin, J.; Wang, S.; Shi, X.; Bao, X., Ti_3C_2 MXene-Derived Sodium/Potassium Titanate Nanoribbons for High-Performance Sodium/Potassium Ion Batteries with Enhanced Capacities. *ACS Nano* **2017,** *11* (5), 4792-4800.
39. Tu, S.; Ming, F.; Zhang, J.; Zhang, X.; Alshareef, H. N., MXene-Derived Ferroelectric Crystals. *Advanced Materials* **2019,** *31* (14), 1806860.
40. Byeon, A.; Hatter, C. B.; Park, J. H.; Ahn, C. W.; Gogotsi, Y.; Lee, J. W., Molybdenum oxide/carbon composites derived from the CO_2 oxidation of Mo_2CT_x (MXene) for lithium ion battery anodes. *Electrochimica Acta* **2017,** *258*, 979-987.
41. Wu, H.; Almalki, M.; Xu, X.; Lei, Y.; Ming, F.; Mallick, A.; Roddatis, V.; Lopatin, S.; Shekhah, O.; Eddaoudi, M.; Alshareef, H. N., MXene Derived Metal–Organic Frameworks. *Journal of the American Chemical Society* **2019,** *141* (51), 20037-20042.
42. Xiao, X.; Wang, H.; Urbankowski, P.; Gogotsi, Y., Topochemical synthesis of 2D materials. *Chemical Society Reviews* **2018,** *47* (23), 8744-8765.
43. Tang, J.; Huang, X.; Lin, T.; Qiu, T.; Huang, H.; Zhu, X.; Gu, Q.; Luo, B.; Wang, L., MXene derived TiS_2 nanosheets for high-rate and long-life sodium-ion capacitors. *Energy Storage Materials* **2020,** *26*, 550-559.
44. He, S.; Zhu, Q.; Soomro, R. A.; Xu, B., MXene derivatives for energy storage applications. *Sustainable Energy & Fuels* **2020**.
45. Kutoglu, A., Kristallstruktur der Calcium-Vanadium-Bronze $Ca_xV^{4+2x}V^{5+2-2x}O_5$. *Zeitschrift für Kristallographie* **1983,** *162* (1-4), 263-272.
46. Ikeda, T.; Boero, M.; Terakura, K., Hydration properties of magnesium and calcium ions from constrained first principles molecular dynamics. *The Journal of Chemical Physics* **2007,** *127* (7), 074503.
47. Wu, M.; Zhang, X.; Gao, S.; Cheng, X.; Rong, Z.; Xu, Y.; Zhao, H.; Huo, L., Construction of monodisperse vanadium pentoxide hollow spheres via a facile route and triethylamine sensing property. *CrystEngComm* **2013,** *15* (46), 10123-10131.
48. Sarycheva, A.; Gogotsi, Y., Raman Spectroscopy Analysis of the Structure and Surface Chemistry of $Ti_3C_2T_x$ MXene. *Chemistry of Materials* **2020,** *32* (8), 3480-3488.
49. Naguib, M.; Mashtalir, O.; Lukatskaya, M. R.; Dyatkin, B.; Zhang, C.; Presser, V.; Gogotsi, Y.; Barsoum, M. W., One-step synthesis of nanocrystalline transition metal oxides on thin sheets of disordered graphitic carbon by oxidation of MXenes. *Chemical Communications* **2014,** *50* (56), 7420-7423.
50. Ahmed, B.; Anjum, D. H.; Hedhili, M. N.; Gogotsi, Y.; Alshareef, H. N., H_2O_2 assisted room temperature oxidation of Ti_2C MXene for Li-ion battery anodes. *Nanoscale* **2016,** *8* (14), 7580-7587.
51. Abello, L.; Husson, E.; Repelin, Y.; Lucazeau, G., Vibrational spectra and valence force field of crystalline V_2O_5. *Spectrochimica Acta Part A: Molecular Spectroscopy* **1983,** *39* (7), 641-651.
52. Petrov, G. I.; Yakovlev, V. V.; Squier, J., Raman microscopy analysis of phase transformation mechanisms in vanadium dioxide. *Applied Physics Letters* **2002,** *81* (6), 1023-1025.
53. Repelin, Y.; Husson, E.; Abello, L.; Lucazeau, G., Structural study of gels of V_2O_5: Normal coordinate analysis. *Spectrochimica Acta Part A: Molecular Spectroscopy* **1985,** *41* (8), 993-1003.
54. Su, Q.; Liu, X. Q.; Ma, H. L.; Guo, Y. P.; Wang, Y. Y., Raman spectroscopic characterization of the microstructure of V_2O_5 films. *Journal of Solid State Electrochemistry* **2008,** *12* (7), 919-923.